GEM NEWS INTERNATIONAL

Contributing Editors
Gagan Choudhary, *IIGJ-Research & Laboratories Centre, Jaipur, India* (gagan.choudhary@iigjrlc.org)
Guanghai Shi, *School of Gemmology, China University of Geosciences, Beijing* (shigh@cugb.edu.cn)

COLORED STONES AND ORGANIC MATERIALS

Emeralds and beryl from Kazakhstan and Ukraine. A set of emeralds and beryl from Kazakhstan and Ukraine were analyzed at GIA's Carlsbad laboratory as part of an ongoing beryl characterization research project. These stones were generously provided by Dr. Gerhard Franz of Technical University Berlin, and Dr. Oleksii Vyshnevskyi of Institute of Geochemistry, Mineralogy and Ore Formation, Ukraine.

Figure 1. Eight Kazakhstani emeralds (left) and three Ukrainian beryl and emerald samples (right), with gemological tweezers shown for scale. The leftmost Ukrainian emerald has a chemistry between that of aquamarine and emerald. Photo by Emily Lane; courtesy of Gerhard Franz and Oleksii Vyshnevskyi.

Editors' note: Interested contributors should contact gandgeditorial@gia.edu.

Gems & Gemology, Vol. 61, No. 2, pp. 206–223.

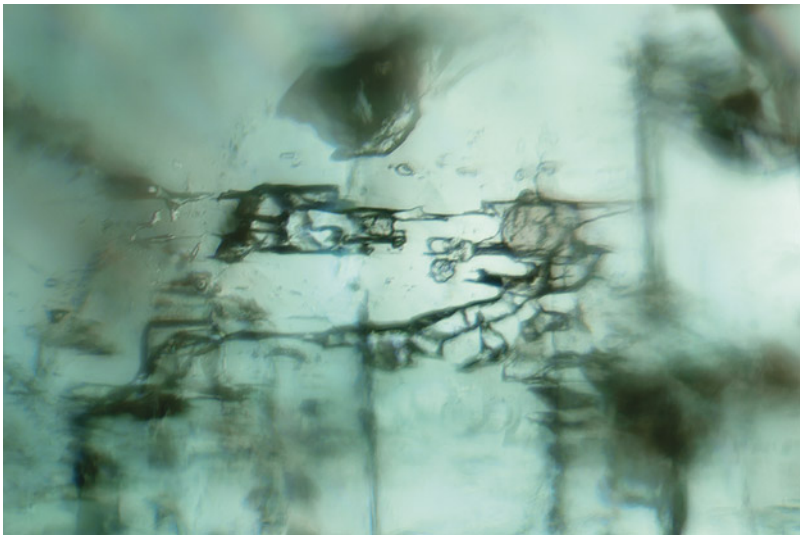

Figure 2. Fluid and two-phase jagged inclusions in a Kazakhstani emerald. Photomicrograph by Rhiana Elizabeth Henry; field of view 1.44 mm.

The study included eight euhedral samples of emerald from the Delbegetey locality in eastern Kazakhstan, and three anhedral beryl and emerald samples from Kruta Balka in southeast Ukraine (figure 1). The Kazakhstani emeralds were light green and had high clarity; they were nearly eye-clean, with small colorless or weakly colored fluid and two-phase inclusions (figure 2). Several had etching and stained surfaces at the base. Due to their high clarity and lively color, they were of gem quality, despite being quite small (only several millimeters in length). The Ukrainian emerald and beryl specimens were bright green and blue-green intergrown anhedral crystals with associated mica, appearing opaque as hand samples.

Chemical analysis by laser ablation–inductively coupled plasma–mass spectrometry (LA-ICP-MS; table 1) revealed distinct compositions based upon a few trace ele-

TABLE 1. Concentrations (in ppm) of significant trace elements in Kazakhstani and Ukrainian emerald and beryl, collected by LA-ICP-MS.

Locality	Mg	Fe	Li	Na	Cs	Cr	V
Kazakhstan	147–302	862–2060	28.7–92.5	316–659	28.7–355	260–716	128–1330
Ukraine	2000–4560	1080–2310	2950–4250	11400–13800	4240–8040	13.5–2000[a]	4.26–26.2
Detection limits (in ppm)	0.05	2	0.04	2	0.03	0.4	0.02

[a]*The chromium concentration of Ukrainian emerald is 631–2000 ppm; the almost-aquamarine has a lower concentration range from 13.5–127 ppm.*

ments, setting them apart from commercially significant deposits. The data also revealed insights into the geological environment in which they formed.

The Kazakhstani emeralds had some of the lowest documented magnesium, iron, and sodium concentrations for emerald, forming a unique data cluster adjacent to that of emeralds from Norway and Nigeria when comparing magnesium and iron (figure 3, left). The Kazakhstani samples were also among the few emeralds with more iron than magnesium, an indicator of their origin at the greisen intersection of the Delbegetey granitic pluton and a Carboniferous sandstone (E.V. Gavrilenko et al., "Emeralds from the Delbegetey deposit (Kazakhstan): Mineralogical characteristics and fluid-inclusion study," *Mineralogical Magazine*, Vol. 70, No. 2, 2006, pp. 159–173), neither of which have significant magnesium to contribute to beryl. While the source of their chromium and vanadium (which contribute to their emerald-green hue in similar proportions) is unknown, some researchers have suggested other regional sedimentary layers as a potential source. Their exceptionally low ratio of magnesium to iron and low but variable cesium to sodium ratio (up to ~0.125 Cs/Na, based on atoms per formula unit) are consistent with formation in a mildly differentiated granite (C. Liu et al., "Continuous Be mineralization from two-mica granite to pegmatite: Critical element enrichment processes in a Himalayan leucogranite pluton," *American Mineralogist*, Vol. 108, No. 2, 2023, pp. 31–41). This formation environment, which is uncommon in emeralds, most closely matches Nigerian emeralds, which have a similar mint green hue.

Figure 3. Chemical comparison of emeralds from economically significant localities, as well as Kazakhstan and Ukraine. Data collected by LA-ICP-MS. Left: The Kazakhstani emeralds (circled) form a distinct cluster at the lower center of the plot. Right: The Ukrainian emeralds (circled) form a distinct cluster at the upper right of the plot.

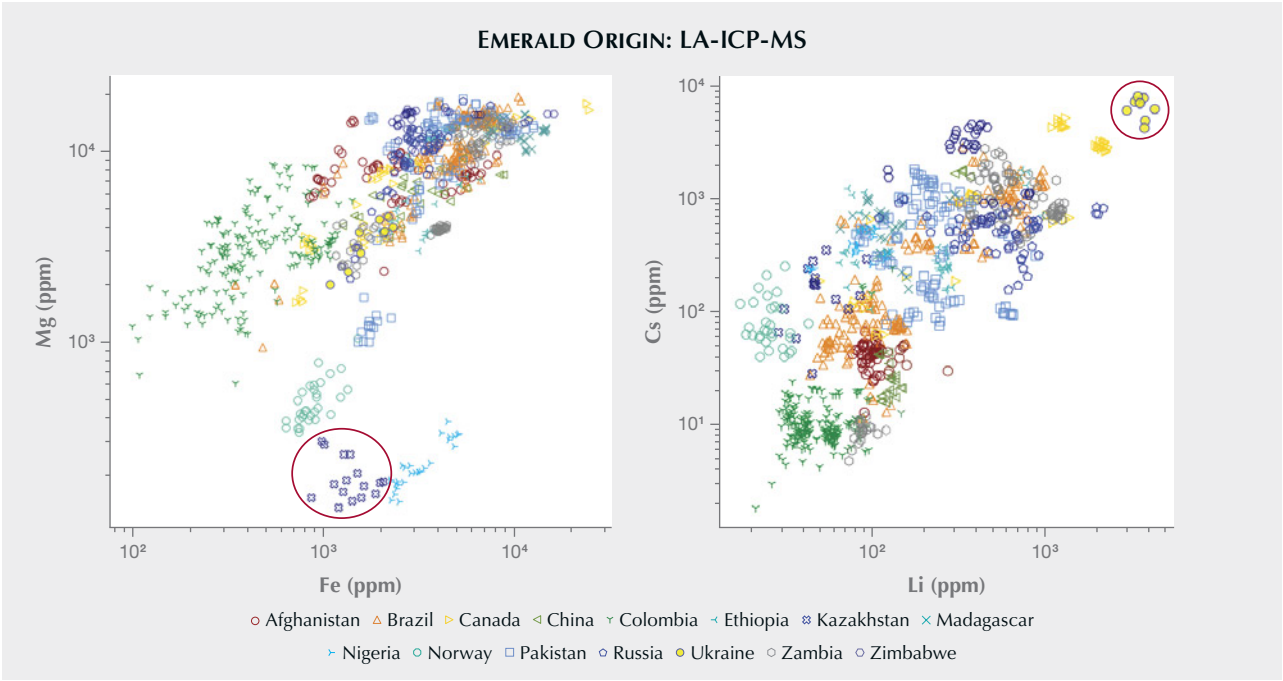

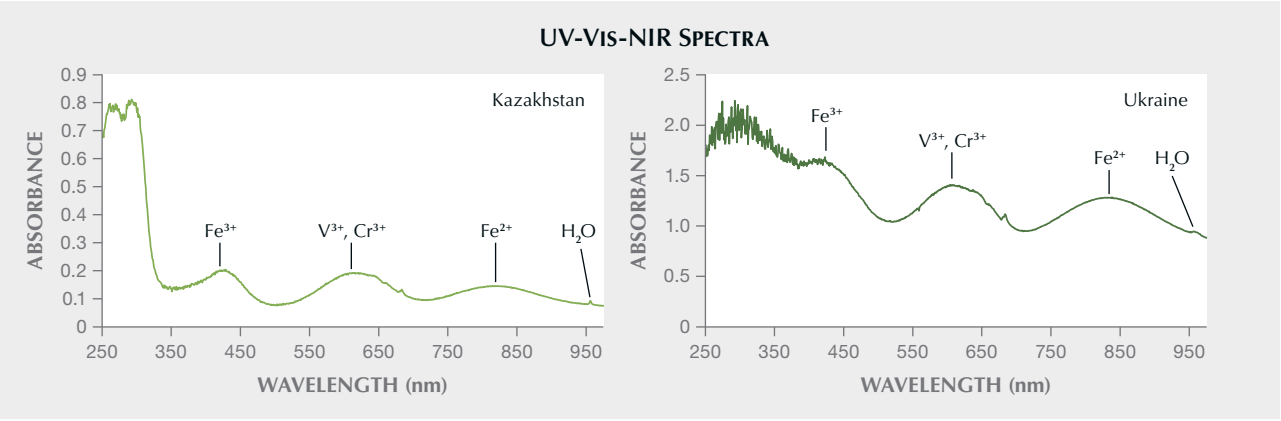

Figure 4. UV-Vis-NIR absorption spectra of a Kazakhstani emerald (left) and a Ukrainian emerald (right). The pale hue is demonstrated by the low absorbance, but the bands clearly show the dominant chromophores and the presence of H_2O, similar to other emeralds.

It is possible that the small size of these emeralds contributes to the perception of paleness, as they have sufficient chromium and vanadium content to provide a distinct green hue that would classify them as emeralds. The ultraviolet/visible/near-infrared (UV-Vis-NIR) spectrum in figure 4 (left) confirms the contribution of these two chromophores.

The Ukrainian beryl and emerald samples are the product of a chemically evolved pegmatite intersecting with an ultramafic host rock, consistent with recent research findings (G. Franz et al., "A new emerald occurrence from Kruta Balka, Western Peri-Azovian region, Ukraine: Implications for understanding the crystal chemistry of emerald," *American Mineralogist*, Vol. 105. No. 2, 2020, pp. 162–181). They had high cesium and lithium (figure 3, right)—higher than what this author recently reported for similar emeralds from Newfoundland, Canada, which form in a similar geological setting (Spring 2024 GNI, pp. 123–125). Only one emerald sample known to the author has had higher cesium content, though it was of uncertain origin, while emeralds from Hiddenite, North Carolina, are rumored to have higher lithium content. The elevated cesium and lithium together are strong indicators of a pegmatitic origin.

The Ukrainian emerald samples had an elevated Cs/Na ratio compared to their Mg/Fe ratio, setting them apart from most other emeralds, though a similar relationship between the two ratios exists in emeralds from Newfoundland, Curlew in Western Australia, and to some extent, Zimbabwe. The green hue of these specimens is attributed more to chromium than vanadium, with a slight influence from iron. The three Ukrainian emeralds also had high zinc compared to other studied emeralds. One had more of a blue hue with lower chromium and vanadium, placing it chemically between an aquamarine and an emerald, but the other two specimens were distinctly emerald based on their significant chromium content and green hue. The UV-Vis-NIR absorption spectrum of one of the green specimens (figure 4, right) confirmed the role of chromium and vanadium in the hue, though the sample's poor transparency contributed to elevated absorbance.

These specimens expand our understanding of emerald beyond the traditional commercial deposits. With their unique characteristics, these two groups push the boundaries of emerald as a beryl variety. Following the present research project, these rare emerald and beryl specimens will join the GIA Museum collection.

Rhiana Elizabeth Henry
GIA, Carlsbad

Unique trapiche grossular from China. Grossular is known in the gem market for its popular varieties, such as tsavorite, hessonite, and rosolite. However, the occurrence of trapiche grossular has rarely been reported. Recently, some previously collected grossular crystals from Hangzhou, Zhejiang Province, China, were found to exhibit a distinct trapiche structure after being cut along specific orientations.

The term *trapiche* refers to a rare growth pattern characterized by radial sector zoning, forming a spoke-like or wheel-shaped appearance. This phenomenon is most commonly observed in emerald, corundum, and tourmaline but has rarely been reported in garnet.

The grossular crystals were collected from a skarn outcrop in southwestern Hangzhou. The formation of skarn is the result of contact metamorphism between granite and limestone. The grossular crystals (figure 5, left) were in the form of rhombic dodecahedrons and appeared black due to a coating of graphite and pyrite. When cut into slices (figure 5, right), they exhibited a colorless and highly transparent appearance. Scanning electron microscopy with energy-dispersive spectroscopy (SEM-EDS) and laser ablation–inductively coupled plasma–mass spectrometry (LA-ICP-MS) analyses indicated their compositions were close to the grossular endmember, with trace amounts of magnesium, titanium, vanadium, chromium, manganese, and iron.

Figure 5. Left: Grossular crystals weighing 0.63 to 4.63 ct from Hangzhou, China. Right: Slices, cut perpendicular to the tetrad axis (top row) and the triad axis (middle and bottom rows). Photos by Hongtao Shen (left) and Tsang Ho Yin (right).

Based on the Raman spectrum and SEM-EDS analyses, the black arms were mainly composed of graphite and possibly other carbonaceous matter (such as bitumen or other amorphous phases). Diopside, fluorapatite, and quartz were also enriched in the arms, which corresponded to boundaries between {110} growth sectors. Furthermore, inclusions were preferentially concentrated along the tetrad and triad axes of the crystals.

The crystals were also fluorescent, showing orangish red under long-wave UV and yellowish orange under short-wave UV. Two main fluorescence centers were identified using 3D fluorescence mapping (not shown). The strongest fluorescence was at ~590 nm in the emission spectra, which is attributed to Mn^{2+}. The weaker fluorescence center in the orange-red region exhibited three sharp peaks centered at 689, 703, and 718 nm, which are usually attributed to Cr^{3+}.

Pyrite, calcite, and zircon were present in almost every sample. Additionally, two rare mineral inclusions, troilite (FeS) and hellandite-Ce, were identified. Troilite was confirmed with SEM-EDS and Raman spectroscopy on polished thin sections; the Fe/S atomic percentage ratio consistently ranged from 0.93 to 0.96. Electron probe microanalysis–wavelength dispersive spectroscopy (EPMA-WDS) analysis was used to identify hellandite-Ce; one calculated chemical formula was $(Ca_{3.66}Y_{0.34})_{\Sigma 4.00}(Ce_{0.71}Nd_{0.37}Y_{0.37}La_{0.30}Sm_{0.07}Pr_{0.07}Gd_{0.05}Dy_{0.05}Eu_{0.04}Tm_{0.02}Er_{0.02}Yb_{0.02}Ho_{0.01})_{\Sigma 2.12}(Al_{0.94}Ti_{0.06})_{\Sigma 1.00}Si_{4.00}B_{4.00}O_{22}(OH)_{1.74}F_{0.03}$. Troilite occurred as particles up to ~800 μm, while hellandite formed druses ranging from 50 to 195 μm. These inclusions occurred randomly within the slices, without a clear association with growth sectors. In some slices, large columnar inclusions were also observed (figure 6), up to 4 mm in length, identified as marialite ($Na_4Al_3Si_9O_{24}Cl$) by Raman and SEM-EDS analyses. Some marialite crystals were partially or completely replaced by a series of common minerals including calcite, diopside, albite, K-feldspar, celsian, prehnite, titanite, and fluorapatite. Celsian ($Ba(Al_2Si_2O_8)$) was also found in some grossular slices and was often associated with K-feldspar with zoning structure resulting from isomorphism. Occasionally, baryte ($BaSO_4$) and alstonite ($BaCa(CO_3)_2$) inclusions could also be detected.

Figure 6. Columnar marialite inclusions in a grossular slice. Photos by Tsang Ho Yin; field of view 0.86 mm (right).

These materials present a new occurrence of a mineral species with a trapiche structure and reflect the unique geological environment of the region as well. The presence of troilite indicates extremely low oxygen fugacity, which suggests a highly reducing environment (X. Li et al., "Thermally induced phase transition of troilite during micro-Raman spectroscopy analysis," *Icarus*, Vol. 390, 2023, article no. 115299). The marialite suggests these grossular garnets may have crystallized from high-salinity hydrothermal fluids (J. Hammerli et al., "Exchange experiments for chlorine and bromine partitioning in scapolite at variable fluid salinities, pressures, and temperatures: Implications for tracing crustal fluid sources via Cl/Br ratios in scapolite," *Contributions to Mineralogy and Petrology*, Vol. 179, 2024, article no. 92). Celsian and some other barium-bearing minerals serve as indicators of an unusual barium-rich environment. Further study of these special inclusions may provide insights into the formation mechanisms of these grossular garnets with fine trapiche textures.

Yinuo Wu, Xingtong Li, and Qian Zhang
Gemological Institute,
China University of Geosciences, Wuhan

Hongtao Shen
State Key Laboratory of Geological Processes and Mineral Resources
China University of Geosciences, Wuhan

Ningyue Sun
Science Research Institute,
China University of Geosciences, Beijing

Zhi Qu
Qingdao Institute of Measurement Technology,
Shandong, Qingdao, China

Ho Yin Tsang
Bedside Mineral Studio, Hong Kong SAR, China

Xiang Pi
Meticulous Minerals, Xiamen, China

GIA 7 Pearl Value Factors: An update on nacre classification. Pearls, both natural and cultured, form in a wide variety of sizes, shapes, and colors. This diversity created the need to distinguish their various appearances, characteristics, and a host of other complex factors that contribute to determining quality, desirability, and ultimately, value. Researching and studying pearls since the 1930s, GIA developed the GIA 7 Pearl Value Factors classification system, a systematic approach to evaluate a pearl's various quality factors through consistent methodology and common terminology (J.W.Y. Ho and S.C. Shih, "Pearl classification: The GIA 7 Pearl Value Factors," Summer 2021 *G&G*, pp. 135–137). The system, which has been widely adopted in the pearl industry, classifies pearls according to size, shape, color, luster, surface, nacre, and matching.

Nacre formation plays a critical role in pearl growth, as its structure influences other value factors such as size, shape, luster, and surface quality. Nacre thickness and continuity also affect a pearl's durability. Prior to this update, a grade of Acceptable denoted expected commercial quality standards, while Unacceptable indicated poor-quality nacre that may impact durability. Prompted by trade requests and feedback, an expansion of the nacre designation for the

Figure 7. Some examples of surface and sub-surface nacre features that impact GIA's new nacre classification scale. A: Near- or sub-surface "hammering." B: "Bubble" appearance shown on the nacre surface. C: Shallow pits or channel depressions giving an "orange peel" effect. D: "Seam" found on a baroque pearl where surface planes meet or change direction and create a peaked ridge. E: "Planar edges" showing subtle angular lines spaced apart across the pearl's surface. F: "Striae" features appearing as flame structures on a nacreous pearl. G: "Sub-surface crack" that may pose a threat to the durability of the pearl. H: An example of a pearl showing both a clean surface and excellent nacre (lacks any visible surface or sub-surface characteristics) based on the GIA 7 Pearl Value Factors. Photos by Emiko Yazawa (A–G) and Eric Welch (H); fields of view 19.27 mm (A and F), 7.19 mm (B), 14.52 mm (C, E, and G), and 9.61 mm (D).

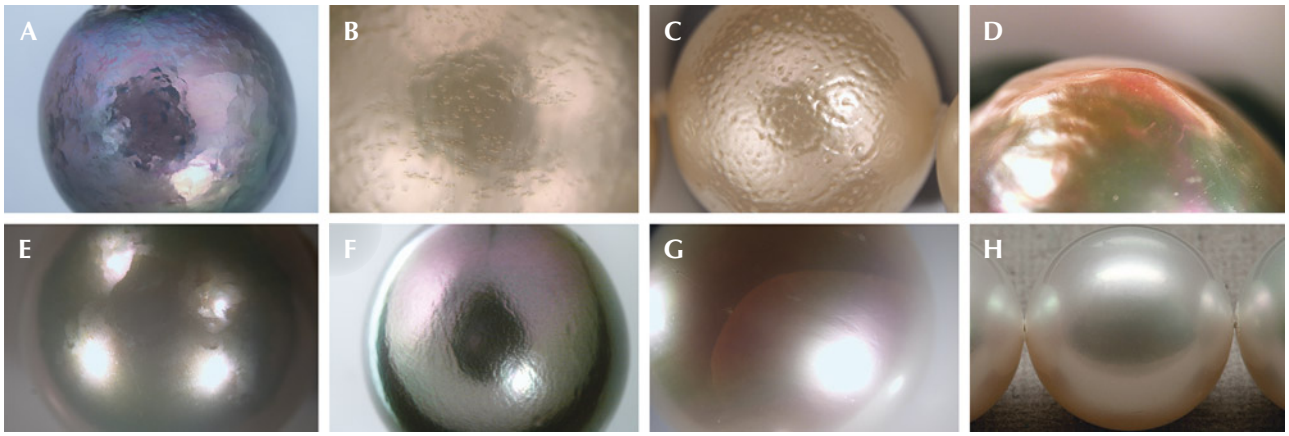

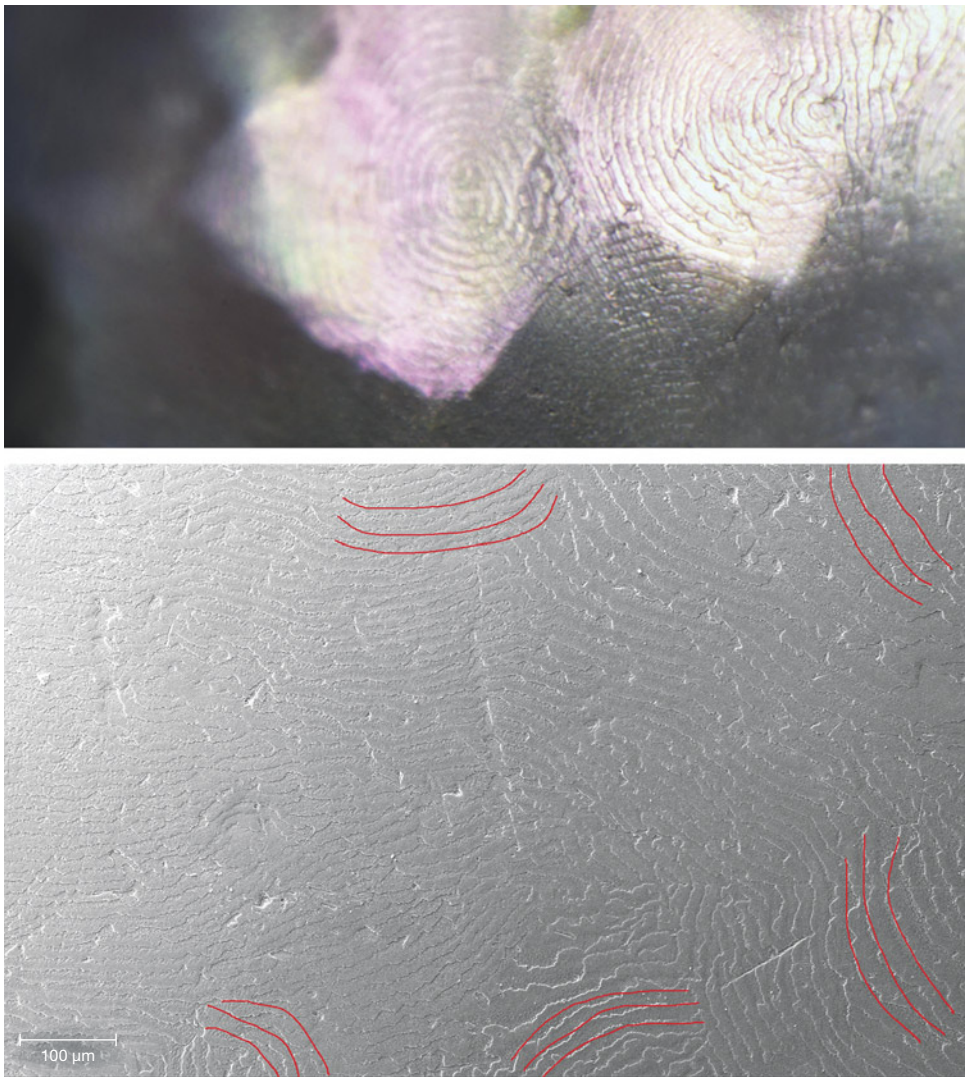

Figure 8. Conventional microscopic (top) and scanning electron microscopic (bottom) observations on the "hammered" surface showed concentric nacre platelet growth patterns on each planar surface. Nacre growth patterns are highlighted in red in the bottom image. Photomicrograph by Chunhui Zhou; field of view 1.40 mm (top).

GIA 7 Pearl Value Factors classification system recently led to the establishment of a new nacre scale more aligned with other quality factors. To implement this change, a detailed investigation was conducted using a variety of pearl samples with surface and sub-surface features indicating various levels of nacre continuity throughout their growth history. As a result, the new nacre scale contains the following five classification ranges: Excellent, Very Good, Good, Fair, and Poor, based on the evaluation of structural or textural nacre features (sometimes referred to as "movement") found either on the surface or sub-surface levels of the pearls. Figure 7 shows some examples of these features and an example free of such features for comparison. Most of the photomicrographs shown in figure 7 magnify the surface features for illustration purposes. The actual classification of pearls is performed by visual observation without magnification under suitable lighting conditions. While "hammering" is a widely known and used term in the industry, GIA has internally assigned specific descriptive names and definitions to other movement types for consistency of identification.

Hammering, named due to its hammered metal appearance (or faceted appearance), exhibits distinct shallow dents or flats that are often seen on baroque pearls but can be present on any shape. This feature can make luster appear softer than it is due to the dispersion of reflections. As a near-surface or sub-surface feature, hammering can often be visible without magnification. Under both conventional microscopic and scanning electron microscopic observations, interesting aragonite nacre platelet structural patterns have been observed in which the nacre on each large planar surface grew concentrically toward its own center (figure 8), as opposed to more integrated and random overlapping nacre platelet structures found on non-hammered pearls. This surface feature is commonly associated with very rapid pearl growth, instead of a growth rate that can provide consistent regular crystal formation for a smooth nacre deposition throughout the whole growth period (J. Taylor and E. Strack, "Pearl production," in P.C. Southgate and J.S. Lucas, Eds., *The Pearl Oyster*, Elsevier, 2008, pp. 273–302).

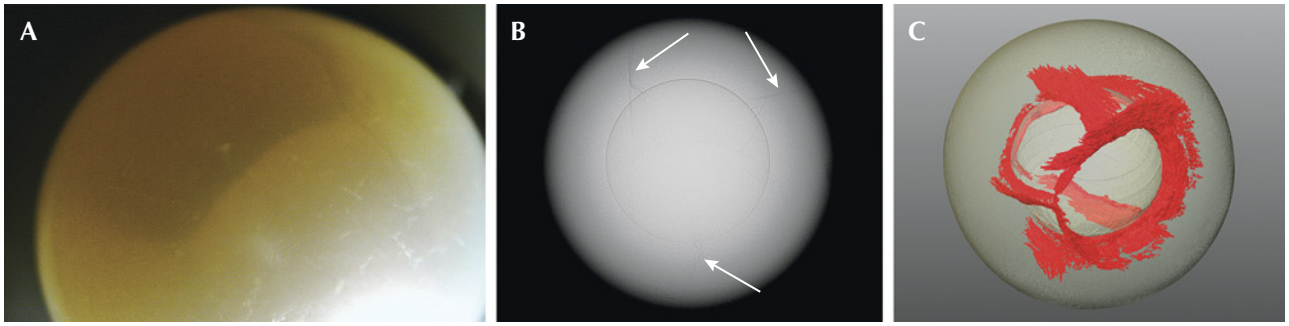

Figure 9. A: A South Sea bead cultured pearl displaying multiple "tideline" features under the surface. Photomicrograph by Emiko Yazawa; field of view 14.52 mm. B: X-ray microradiograph of the pearl showing the cracks (indicated by arrows) extending from the bead nucleus toward the surface. C: 3D reconstruction using X-ray computed microtomography data generated an overall 3D representation of the distribution of the internal cracks (in red).

Another feature commonly seen on some pearls is the internal fissures or cracks not far below the nacre surface that can be observed under strong lighting conditions (sometimes referred to as "tidelines"). Figure 9 presents a good example of such a feature: a South Sea bead cultured pearl containing multiple internal cracks beneath the nacre surface. Under X-ray radiographic examination, these internal cracks can extend toward different directions between the bead nucleus and the nacre surface. 3D reconstruction of the X-ray computed microtomography data showed the extent of these cracks radiating from the bead nucleus, providing a better visualization of how these internal fissures are distributed and interconnected with each other (see video at https://www.gia.edu/gems-gemology/summer-2025-gemnews-gia-7-pearl-value-factors-update-nacre-classification). While drilling may occasionally cause internal cracks, undrilled pearls such as this example could also display these growth disruptions within their nacre layers, which may pose durability issues. The exact cause of this feature on undrilled pearls remains unknown.

In summary, the new nacre continuity classification range characterizes the degree of surface or sub-surface nacre disruption, with the baseline being a perfectly smooth, uninterrupted (i.e., Excellent) nacre. Additionally, each cultured pearl type has a minimum parameter for nacre thickness. Based on our observations, most cultured pearls of commercial grade fall into the Good nacre quality range, as opposed to the previous grade of Acceptable, while pearls of higher quality may reach Very Good or Excellent. This update on the nacre quality scale provides improvement to the existing nacre quality description for the GIA 7 Pearl Value Factors classification system.

Akira Hyatt, Emiko Yazawa, and Chunhui Zhou
GIA, New York

Exceptional nacre thickness of hybrid akoya bead cultured pearls. Akoya pearl farming was established in Japan more than a century ago and subsequently expanded to other countries such as China, Vietnam, and Australia. The akoya pearl oyster includes members of mollusks that

Figure 10. Group of 81 hybrid akoya bead cultured pearls ranging from 4.00 × 3.93 mm to 6.44 × 6.28 mm. Photo by Nuttapol Kitdee.

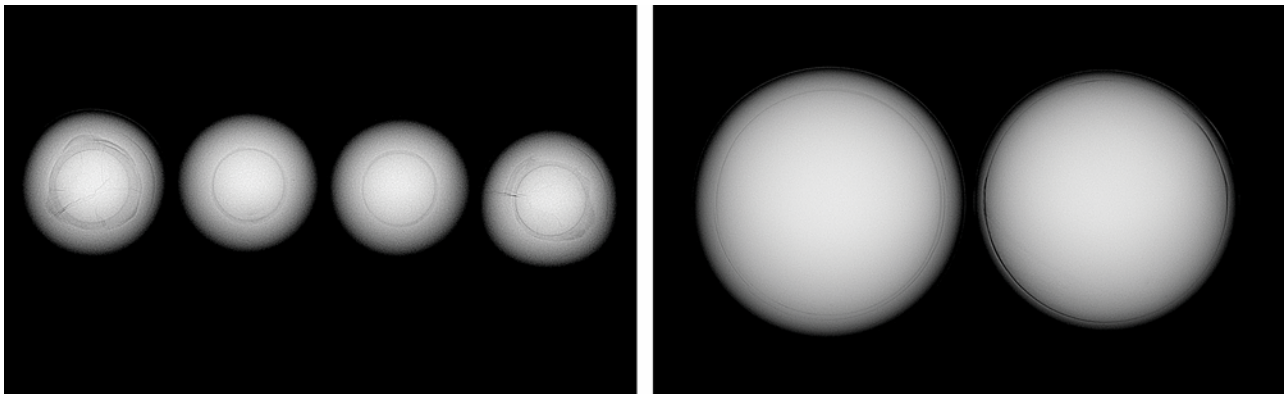

Figure 11. Left: RTX images of the four 6 mm pearls show round bead nuclei and dark gray areas around the beads associated with organic-rich material. Nacre thickness of each pearl from left to right: 1.67, 1.68, 1.62, and 1.64 mm, respectively. Right: The nacre overgrowths are significantly thicker than those of typical akoya pearls, such as the two shown here.

belong to the *Pinctada fucata*, *martensii, radiata*, and *imbricata* species complex (K.T. Wada and I. Tëmkin, "Taxonomy and phylogeny," in P.C. Southgate and J.S. Lucas, Eds., *The Pearl Oyster*, Elsevier, Oxford, 2008, pp. 37–75). The *P. fucata* (*martensii*) is the most widely used species to produce akoya cultured pearls.

Akoya bead cultured (BC) pearls are characterized by their round shapes and high luster. The growth period typically ranges from 10 to 14 months, which is shorter than that of South Sea (*P. maxima*) and Tahitian (*P. margaritifera*) BC pearls. A longer growth time can possibly impact the roundness of the pearls. Akoya mollusks can produce high-quality nacre when the water temperature is between 15° to 20°C, as cool water slows the rate of nacre deposition. Due to the shorter growth period and lower temperature growth conditions, akoya BC pearls are generally known to have a thinner nacre overgrowth than South Sea and Tahitian BC pearls. This also implies that a uniform white shell bead with no discoloration must be used during the nucleation process since low-quality beads can affect the quality of the final pearls (N. Sturman et al., "Vietnam: Shell nuclei, pearl hatcheries, and pearl farming," Fall 2020 *G&G*, pp. 402–415). Very thin nacre can impact the durability and luster of pearls. As a result, many pearl farmers continually refine their techniques to achieve the highest quality with respect to shape, luster, and nacre thickness on their final products while balancing culturing time and cost.

GIA's Bangkok laboratory received 91 hybrid akoya bead cultured pearls for study, weighing a total of 53.54 carats and ranging from 4.00 × 3.93 mm to 6.44 × 6.28 mm in diameter, from Orient Pearl (Bangkok) Ltd (figure 10). Reportedly produced at a pearl farm in Nha Trang, Vietnam, the pearls were harvested in April 2023 from hybrid mollusks that were crossbred between *P. fucata* (*martensii*) and *P. radiata* species. These akoya pearls are said to have a thicker nacre than typical akoya BC pearls produced from pure *P. fucata* (*martensii*) species, as the hybrid mollusks are more tolerant of warmer water, and therefore the nacre of their pearls can grow faster. However, only a very small percentage (around 0.5%) of the total production of these hybrid mollusks yields pearls with nacre significantly thicker than those from pure *P. fucata* mollusks. Traditional American freshwater shell beads were used to grow the pearls, with a cultivation period of only 5 months for the 4 mm pearls and about a year for the 6 mm pearls.

Most of the samples (87 out of 91) were about 4 mm in diameter, and the other four samples were 6 mm. All pearls were round with predominantly cream color, most having noticeable orient and pink and green overtone. They all had fine nacre, with no evidence of processing or color enhancement on their surfaces. The pearls fluoresced a very weak to moderate yellowish green under long-wave UV light. Short-wave UV fluorescence spectroscopy with 275 nm LED excitation resulted in counts of high intensity for these pearls, indicating that they were naturally colored and lacked the processing routinely applied for akoya pearls (Spring 2020 Lab Notes, p. 136). Ultraviolet/visible spectroscopy revealed absorption features around 435 and 460 nm in some of the pearls, which are characteristic features reportedly found on *P. radiata* pearls (A. Al-Alawi et al., "Saltwater cultured pearls from *Pinctada radiata* in Abu Dhabi (United Arab Emirates)," *Journal of Gemmology*, Vol. 37, No. 2, 2020, pp. 164–179).

Real-time X-ray microradiography (RTX) analysis revealed that each pearl showed a thick nacre layer with a round bead nucleus in the center. Some of the beads were surrounded by an organic-rich material, as evidenced by dark gray areas with RTX. X-ray radiography was used to obtain the measurements. The four 6 mm pearls had a nacre thickness between 1.62 to 1.68 mm (figure 11, left), significantly thicker than the typical nacre range of 0.15 to 0.50 mm in traditional akoya pearls (figure 11, right). Nacre thickness of the 4 mm pearls ranged from 1.11 to 1.46 mm.

The degree of X-ray fluorescence (XRF) reaction observed in saltwater BC pearls is dependent on nacre thickness. Freshwater shell beads exhibit a high intensity of greenish

TABLE 1. Measurements of nacre thickness and diameter of the pearl and bead obtained by RTX analysis. Volume ratios of the bead and nacre to the total volume of the pearl can be calculated based on the equations presented.

Pearl	Nacre thickness (mm)	Diameter (mm)		Volume ratio	
		Pearl (*D*)	Bead (*d*)	Bead $(d/D)^3$	Nacre (*1 – Bead volume ratio*)
1	1.67	6.30	2.97	0.11	0.89
2	1.68	6.33	2.89	0.10	0.90
3	1.62	6.25	2.93	0.10	0.90
4	1.64	6.14	2.86	0.10	0.90

yellow fluorescence due to trace amounts of manganese, while nacre produced in saltwater is generally inert. Thin nacre often allows a bead's fluorescence to pass through, resulting in the pearl displaying noticeable fluorescence. Due to their thick nacre, the four hybrid akoya pearls either exhibited weak fluorescence or were inert to XRF.

Additionally, the diameters of the pearl (*D*) and bead (*d*) can be used to calculate the ratios of both nacre volume and bead volume to total pearl volume, as illustrated in table 1. From the calculation, all four 6 mm pearls have a high percent nacre volume of around 90% of the total pearl volume. Therefore, the bead nucleus only occupies around 10% of the total pearl volume. The nacre volume of all 4 mm pearls ranged from 90–94% of the total pearl volume.

For additional study, two of the 6 mm pearls were selected for X-ray computed microtomography (μ-CT) analysis. Specialized software to render the μ-CT scan images was used to generate three-dimensional models and measure nacre thickness and volume percentage of the pearl nacre and the bead. The results obtained were consistent with the calculation results from RTX analyses (table 2).

This study demonstrated that the hybrid mollusk species of *P. fucata* (*martensii*) and *P. radiata* can produce BC pearls with a thick nacre layer with the nacre accounting for approximately 90% of the total pearl volume. Furthermore, according to the GIA 7 Pearl Value Factors classification system, the hybrid pearls studied displayed Excellent and Very Good lusters. Therefore, the

TABLE 2. Results from μ-CT and RTX analyses comparing nacre thickness, bead and nacre volumes, and their percent of total pearl volumes for the two 6 mm pearls.

Pearl	μ-CT 3D model	Nacre thickness (mm)		Bead volume		Nacre volume	
		RTX	μ-CT	RTX	μ-CT	RTX	μ-CT
1	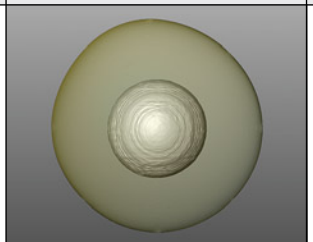	1.67	1.67	13.814 mm³ 11%	12.986 mm³ 10%	116.690 mm³ 89%	113.218 mm³ 90%
2	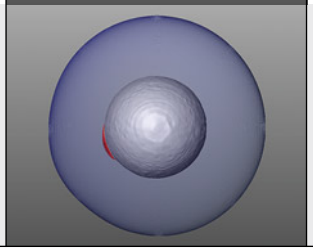	1.68	1.68	12.730 mm³ 10%	11.956 mm³ 10%	119.047 mm³ 90%	106.530 mm³ 90%

thick and fine quality of the nacre resulted in high luster. A sufficient nacre layer can enhance durability, which is an essential characteristic that contributes to the value and beauty of akoya BC pearls.

Kwanreun Lawanwong and Ravenya Atchalak
GIA, Bangkok

Emiko Yazawa
GIA, New York

Iridescent gems cut from hinge ligament of South Sea pearl oyster (*Pinctada maxima*). Pearl oysters of the *Pinctada* genus are known to produce beautiful nacreous pearls (*The Pearl Blue Book*, CIBJO, 2022). The iridescent nacre of their shells, known as mother-of-pearl, is often used as a gem material. Another part of the oyster—the hinge ligament—also can be used as a gem material. The hinge ligament is a mineralized tissue that connects the two shells of a bivalve mollusk.

Shoji Naito, a Tokyo-based lapidary with more than forty years of experience in gemstone cutting, had a large South Sea pearl oyster (*Pinctada maxima*) shell that he kept for at least 37 years. The cross section of the shell's thick hinge ligament displayed iridescence. To enhance this attractive phenomenon, the hinge ligament was cut and polished into cabochons, a practice that has remained unknown in the gem industry. Author YK recently purchased one of these cabochons: a 0.72 ct black opaque specimen.

Due to the item's appearance, particularly its greasy luster and iridescence, the cabochon can be confused with other iridescent materials such as opal imitations. Since this unique material has yet to be studied in detail, Naito loaned rough and polished cabochon ligaments as well as the shell (figure 12) to GIA for gemological examination.

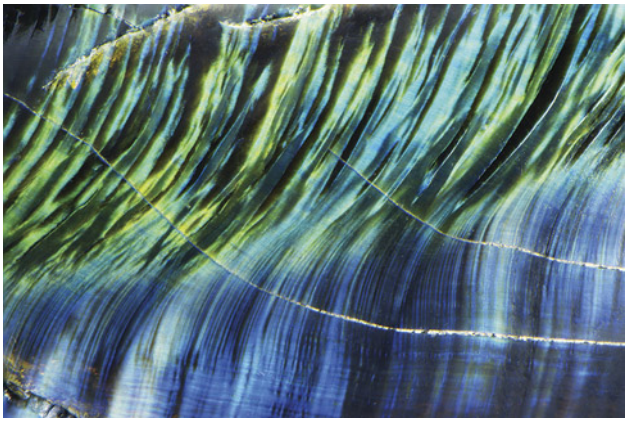

Figure 13. An iridescence on the cross-section surfaces of a hinge ligament fragment from the South Sea pearl oyster. Photomicrograph by Nathan Renfro; field of view 3.60 mm.

The 0.72 ct cabochon had a refractive index of 1.560 (spot reading) and a hydrostatic specific gravity (SG) of 1.18. The very low SG of this cabochon compared to pearls or shells, which are generally above 2.60, indicated that it contained a higher percentage of organic material. Microscopic observation revealed fibrous structures with iridescent reflections. The fibrous structures displayed a wavy pattern of blue/green-dominant iridescence against the black opaque matrix. Rough fragments showed the same patterns at the cross sections (figure 13).

In addition to standard gemological testing and observations, more advanced testing methods were applied to

Figure 12. Polished and unpolished hinge ligaments with a Pinctada maxima *shell. Photo by Annie Haynes.*

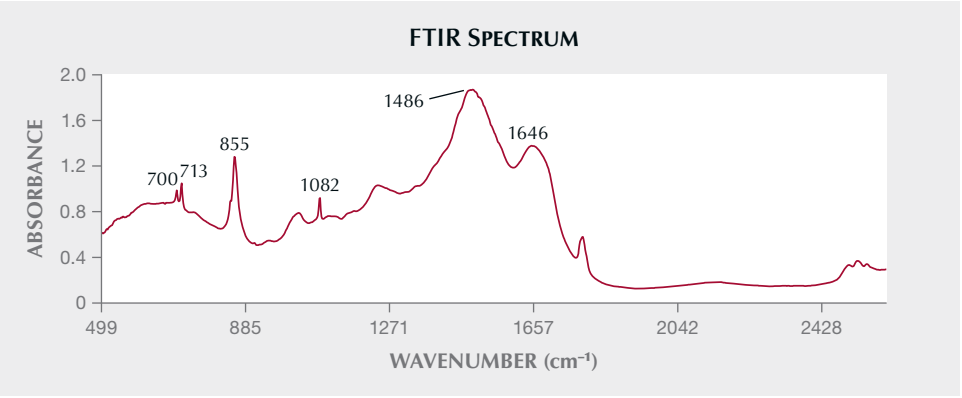

Figure 14. The FTIR spectrum revealed aragonite peaks at 1486, 1082, 855, 713, and 700 cm^{-1}, together with an amide I peak that is associated with conchiolin at 1646 cm^{-1}.

the fragment and polished samples at GIA's laboratory in Carlsbad. Raman spectroscopy with 830 nm laser excitation clearly detected aragonite peaks (1086, a doublet at 702 and 706, 206, and 152 cm^{-1}). The ultraviolet/visible/near-infrared (UV-Vis-NIR) reflectance spectra showed an absorption at 280 nm associated with conchiolin. For collecting Fourier-transform infrared (FTIR) spectra, two KBr pellets were prepared with powders collected from ligament fragments. The FTIR spectra (figure 14) showed aragonite peaks (1486, 1082, 855, 713, and 700 cm^{-1}) and an amide I peak at 1646 cm^{-1} related to conchiolin, which are identical to the spectrum reported for the ligament of the akoya pearl oyster (*P. fucata*) (M. Suzuki et al., "A unique methionine-rich protein-aragonite crystal complex: Structure and mechanical functions of *Pinctada fucata* bivalve hinge ligament," *Acta Biomaterialia*, Vol. 100, 2019, pp. 1–9).

Energy-dispersive X-ray fluorescence (EDXRF) spectroscopy showed very high calcium (397300 ± 1600 ppm), low levels of manganese (110 ± 42 ppm), and high strontium (3077 ± 89 ppm) contents for the 0.72 ct cabochon, confirming calcium carbonate material of saltwater origin. The results for the fragments also showed the same trend. Laser ablation–inductively coupled plasma–mass spectroscopy (LA-ICP-MS) analysis confirmed the EDXRF results. Furthermore, most trace elements exhibited concentrations comparable to previously reported nacreous *P. maxima* pearls (e.g., K. Scarratt et al., "Natural pearls from Australian *Pinctada maxima*," Winter 2012 *G&G*, pp. 236–261; N. Sturman et al., "Bead-cultured and non-bead-cultured pearls from Lombok, Indonesia," Fall 2016 *G&G*, pp. 288–297). The magnesium level was significantly higher, however, which is likely related to the organic-rich nature of the material.

Real-time X-ray microradiography (RTX) revealed that both the cabochons and fragments exhibited a similar banded structure alternating between light gray and dark gray stripes. The light gray areas appeared to be dense aragonite material that was generally more radiopaque than the dark gray areas of protein-rich materials (figure 15). Cracks were presented as darker gray lines across the structure. The internal banded structure corresponds to the arrangement of the fibers creating the iridescent effect.

The hinge ligaments of Tahitian pearl oyster (*P. margaritifera*) shells from GIA's research collection were also tested for comparison. Due to the smaller size of the *P. margaritifera* shell, the hinge ligaments are thinner and display less iridescence than the *P. maxima* sample studied. However, the testing results were consistent.

This study showed that FTIR (KBr pellet) analysis can be used, in addition to standard gemological testing and microscopic observations, to verify the characteristic aragonite and amide I peaks of the hinge ligament. However, KBr pellet analysis is destructive—Raman and UV-Vis-NIR reflectance spectroscopies and RTX analysis should be attempted first.

This unique biogenic material from pearl oysters can potentially produce a new eye-catching blue-green iridescent gem material.

Yusuke Katsurada
GIA, Tokyo

Artitaya Homkrajae and Amiroh Steen
GIA, Carlsbad

Figure 15. The 0.72 ct cabochon showed an internal banded structure alternating between light gray stripes of aragonite and dark gray stripes of protein-rich material in the RTX image. Image by Amiroh Steen.

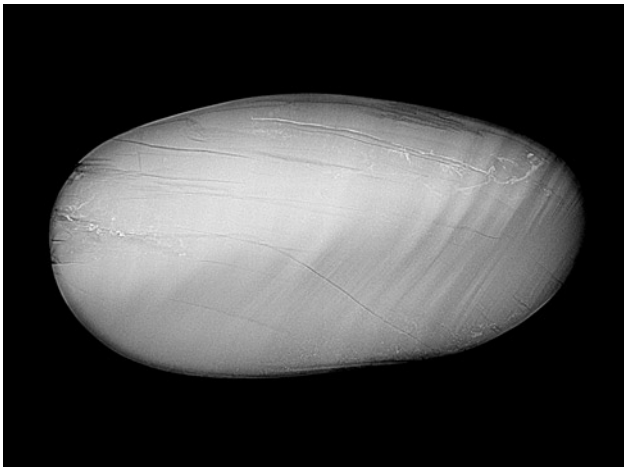

Figure 16. This 0.20 ct faceted transparent, colorless poudretteite measures 3.48 × 4.06 mm. Photo by Jianxing Wang.

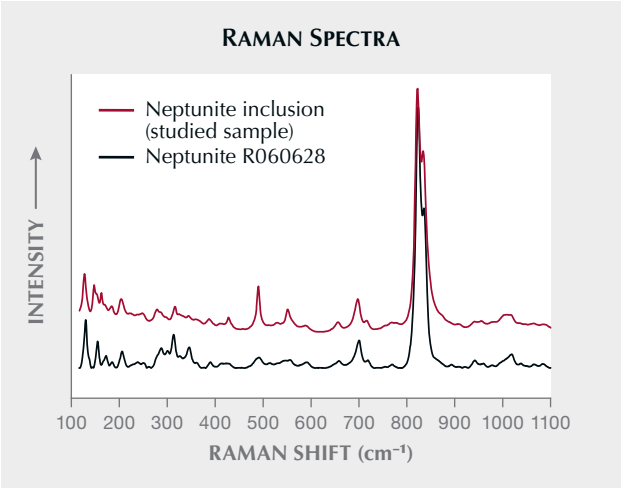

Figure 18. Raman spectrum of the neptunite inclusion in the poudretteite compared to that of a RRUFF reference spectrum. Spectra are offset vertically for clarity.

Neptunite inclusions in rare poudretteite. The authors recently found a 0.20 ct faceted transparent, colorless poudretteite (figure 16) resembling colorless spinel or taaffeite at a jewelry market in China's Yunnan Province. Poudretteite is a rare hexagonal silicate gemstone variety with the chemical formula $KNa_2(B_3Si_{12})O_{30}$ (J.D. Grice et al., "Poudretteite, $KNa_2(B_3Si_{12})O_{30}$, a new member of the osumilite group from Mont Saint-Hilaire, Quebec, and its crystal structure," *Canadian Mineralogist*, Vol. 25, No. 4, 1987, pp. 763–766). It is found primarily in the Quebec province of Canada and in Mogok, Myanmar (C.P. Smith et al., "Poudretteite: A rare gem species from the Mogok Valley," Spring 2003 *G&G*, pp. 24–31). Northern Myanmar, which borders China's Yunnan Province, is perhaps the most likely origin of this sample. Standard gemological testing revealed a refractive index of 1.513–1.533 and a hydrostatic specific gravity of 2.51. The stone was uniaxial positive, and its ultraviolet fluorescence was inert. Raman spectroscopy confirmed the sample was poudretteite.

Three reddish brown crystal inclusions were observed within the stone (figure 17). Raman spectroscopy identified them as the rare mineral neptunite ($KNa_2Li(Fe^{2+},Mn)_2Ti_2Si_8O_{24}$) (figure 18; B. Lafuente et al., 2015, https://rruff.info/about/downloads/HMC1-30.pdf), which has been found in Greenland, Canada, and the United States (Summer 2021 *G&G* Micro-World, pp. 160–161). To the best of our knowledge, this is the first recorded occurrence of neptunite inclusions in poudretteite.

Jianxing Wang
Jewelry Testing Center,
Shenzhen Polytechnic University, China

Kong Gao
College of Jewelry,
Guangzhou Panyu Polytechnic, China

Figure 17. One of the reddish brown neptunite inclusions in the poudretteite. Photomicrograph by Jianxing Wang; field of view 1.50 mm.

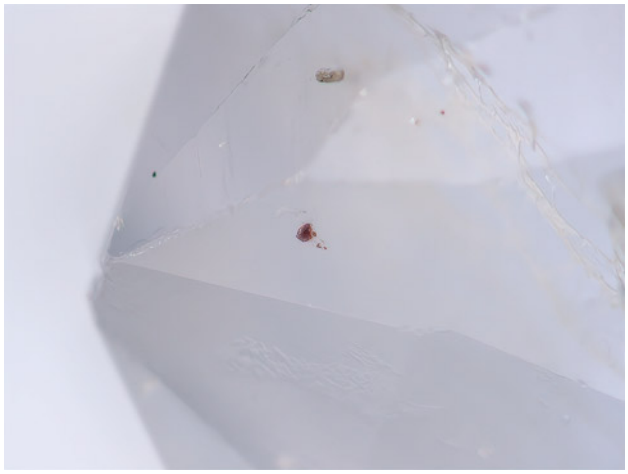

New väyrynenite production from Nigeria. Väyrynenite was officially described as a mineral in 1954, based on samples from the Viitaniemi pegmatite field in central Finland. The rare phosphate mineral ($BeMn^{2+}(PO_4)(OH)$) was named after professor H.A. Väyrynen. Nearly all the material was initially found as opaque, fine-grained aggregates, lacking any euhedral crystal formation.

It wasn't until the 1970s that the mineral gained popularity with the discovery of well-formed crystals in the Chitral area of Pakistan. Initially, most of the interest was in mineral specimens. Occasionally, material suitable for faceting was recovered, but it was often included and limited to sizes under 1 carat, making väyrynenite a true collector's stone. Some small faceted material was recently reported from Afghanistan as well (Spring 2025 GNI, p. 102).

Figure 19. Nigerian väyrynenite vary from orange to orangy pink colors and occur in high clarity. These stones range from 0.72 to 2.45 ct. Photo by Nuttapol Kitdee; courtesy of Thai Lanka Trading.

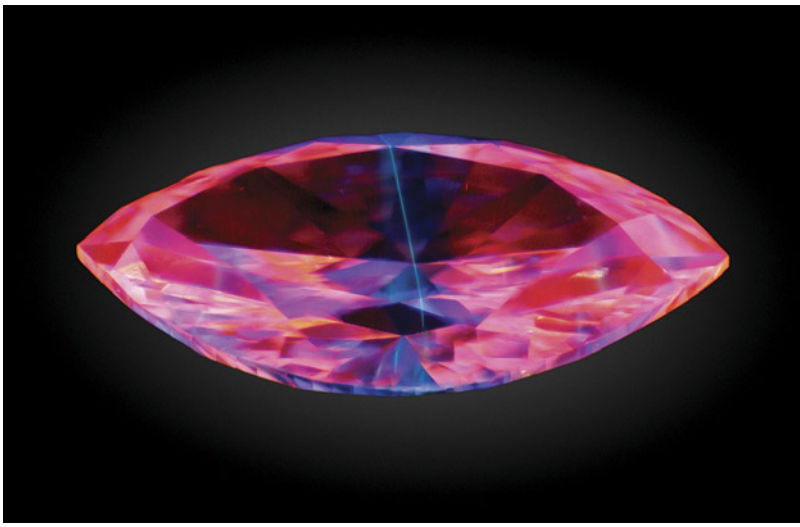

Figure 20. Deep-UV imaging of the 0.07 ct multilayered laboratory-grown diamond (4.20 × 2.26 × 1.27 mm) showing fluorescence of a thin blue-green layer between two pink-orange CVD layers. Image by Sean O'Neal.

Since fall 2024, larger stones have been seen in the trade, including multiple clean faceted gems over 10 ct. These are reportedly from Nasarawa State in Nigeria, near the village of Angwan Doka, roughly 20 km southeast of the city of Keffi. The area around Keffi is well known for pegmatite-related gems, especially pink, green, and bicolor tourmalines. In mid-2024, at a site previously mined for tourmaline, artisanal miners struck a pocket of unknown orange to orangy pink material later identified as väyrynenite. Väyrynenite occurs as an alteration product in certain types of pegmatites.

GIA recently studied a set of stones, weighing 0.72 to 2.45 ct, from the new Nigerian source loaned from Mark Smith of Thai Lanka Trading in Bangkok (figure 19). All properties matched previously known väyrynenite: refractive index of 1.639–1.676 with a birefringence ranging from 0.025–0.027, biaxial optical figure, and a density of 3.22–3.25. Its orangy pink color sometimes ranged into a pure orange. Using a dichroscope, the stones showed trichroism (pinkish orange–pure pink–yellowish orange). None of the stones showed fluorescence under long-wave (365 nm) or short-wave (254 nm) UV. Raman spectroscopy confirmed their identity as well.

All stones were eye-clean but showed strong doubling of the pavilion facets under 10× magnification. Inclusions were limited to healed fractures with two-phase fluid inclusions.

While its mineral properties and colors are similar to those of the Pakistani material, the new material from Nigeria exhibits larger crystal sizes and higher clarities. This is exciting news for the gem world, where väyrynenite is becoming more accessible in higher qualities.

Wim Vertriest
GIA, Bangkok

DIAMONDS

Multilayered laboratory-grown diamond. A marquise-shaped laboratory-grown diamond weighing 0.07 ct and measuring 4.20 × 2.26 × 1.27 mm was recently submitted to Stuller's gemological laboratory for testing. The near-colorless (G–H color range) and very slightly included (VVS_2–VS_1) stone provided some unusual results.

Deep-UV excitation (<225 nm) of the laboratory-grown diamond produced a multicolored pink-orange fluorescence accented by the dislocation bundles' vein-like

Figure 21. Short-wave UV imaging of the multilayered laboratory-grown diamond showed the thin layer phosphorescing while the rest of the diamond remained inert. Image by Guy Borenstein.

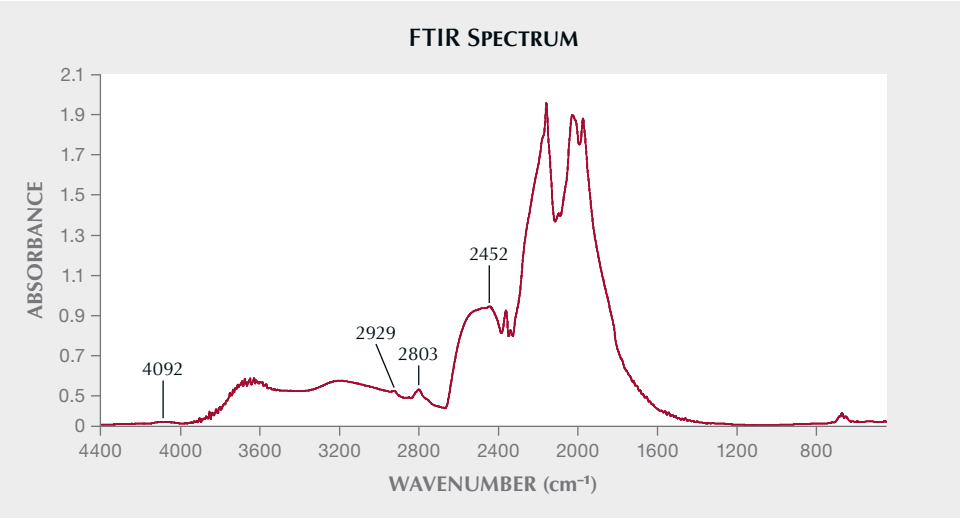

Figure 22. FTIR spectrum of the laboratory-grown diamond showing uncompensated boron at 4092, 2929, 2803, and 2452 cm^{-1}.

pattern toward the long pointed edges and a thin (<50 µm) greenish blue layer crossing the center of the stone vertically from the table facet to the pavilion (figure 20). Viewed separately using broad-range pulsed xenon (120–2000 nm) and short-wave UV (254 nm) imaging, it exhibited a persistent (>5 s) zone of greenish blue phosphorescence in the same location as the previously mentioned greenish blue fluorescent layer (figure 21).

When viewed with crossed polarizing filters, a strain in columnar and cross-hatched patterns was easily observed, though a thin layer of dark solid color was also observed. The section with the solid strain was once again consistent with the area of fluorescence and phosphorescence. Infrared spectroscopy revealed indications of uncompensated boron at 4092, 2929, 2803, and 2452 cm^{-1}, and no nitrogen was detected (figure 22). Photoluminescence (PL) spectroscopy under liquid nitrogen (77K, –196°C), using 532 nm laser excitation, showed differences between areas within the stone. When the laser was focused on the long edges, sharp peaks at 575 and 637 nm (the NV^0 and NV^- centers, respectively) were observed, with the former being stronger. The NV^0 and NV^- centers are shown in figure 23, labeled "side A" and "side B," respectively. Also, weak SiV^- lines at 737 nm were detected on both edges. When the laser was focused on the thin layer labeled "center" in figure 23, the NV^0 and NV^- zero-phonon lines were significantly reduced and no SiV^- was detected.

The distinctive fluorescence and phosphorescence patterns observed under deep-UV, short-wave UV, and xenon imaging, as well as the presence of zonal dislocation bundles, strain characteristics, and PL spectra differences, suggest a complex growth process involving multiple layers.

NV^0 causes orange-red fluorescence in deep UV, a typical property of diamonds grown by chemical vapor deposition (CVD) without post-growth high-pressure, high-temperature (HPHT) treatment (P.M. Martineau et al.,

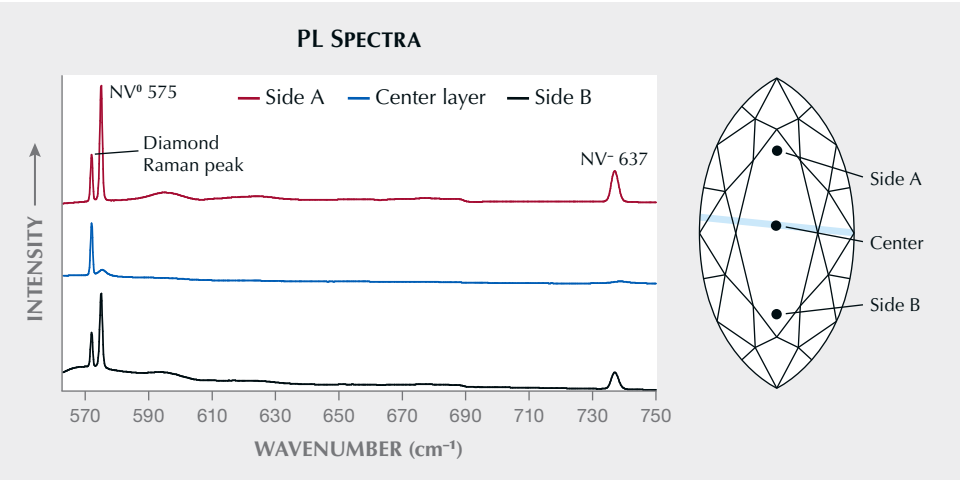

Figure 23. PL spectra of three areas within the laboratory-grown diamond. Sides A and B display a similar pattern with strong NV^0 and NV^- peaks at 575 and 637 nm, respectively. The center layer (<50 µm) shows a different response, with much lower intensities. Spectra are offset vertically for clarity.

"Identification of synthetic diamond grown using chemical vapor deposition," Spring 2004 *G&G*, pp. 2–25). The green-blue fluorescence and long-term phosphorescence reaction to deep UV is associated with both HPHT-grown and CVD-grown diamonds, while the infrared spectrum and long-term phosphorescence under short-wave UV are associated with boron impurities. These features are typical properties of HPHT-grown diamonds (C.M. Welbourn et al., "De Beers natural versus synthetic diamond verification instruments," Fall 1996 *G&G*, pp. 156–169; K. Watanabe et al., "Phosphorescence in high-pressure synthetic diamond," *Diamond and Related Materials*, Vol. 6, No. 1, 1997, pp. 99–106), but can also point to the phosphorescence seen in boron-incorporated type IIb CVD-grown products and interfaces between CVD growth layers (S. Eaton-Magaña et al., "Observations on HPHT-grown synthetic diamonds: A review," Fall 2017 *G&G*, pp. 262–284; S. Eaton-Magaña, "Summary of CVD lab-grown diamonds seen at the GIA laboratory," Fall 2018 *G&G*, pp. 269–270; S. Eaton-Magaña et al., "Laboratory-grown diamonds: An update on identification and products evaluated at GIA," Summer 2024 *G&G*, pp. 146–167).

The strain shown in two patterns on each side of the stone was consistent with CVD growth (E. Fritsch et al., "'Birefringence' in diamond: A useful tool to separate natural from synthetic diamond," *32nd International Gemmological Conference* IGC. Interlaken, Switzerland, July 13–17, 2011, pp. 71–72). However, the pattern difference indicates that each layer was created separately. In addition, the thin layer in the center showed a dark solid strain. This layer's dark appearance could be due to an elastic strain applied to the neighboring layers, possibly masking a thin, strain-free area commonly observed in HPHT-grown diamonds.

Infrared spectroscopy using the DRIFT technique confirmed a type IIb diamond structure, mostly typical of colorless to near-colorless HPHT-grown diamonds (Eaton-Magaña et al., 2017) or boron-incorporated type IIb CVD-grown diamond (Eaton-Magaña et al., 2024). Also, the nitrogen vacancies' peak changes between layers, observed using PL, could be the result of an HPHT process in the center thin layer or different growth conditions in the CVD feed gas during start-stop cycles (Eaton-Magaña, 2018). Considering the relatively high boron detected, contamination due to HPHT annealing seems unlikely. Hence, the center layer was either grown using an HPHT method or formed as a boron-rich CVD layer during a multi-stage growth.

These results highlight the stone's heterogeneous composition. The findings suggest a multilayered synthetic diamond, with either three distinctly different CVD growth layers or two CVD layers on both ends of the stone and a thin HPHT layer between them. This case highlights the challenges of discerning the intricacies of diamond synthesis. As more consumers request a specific growth method and gemological laboratories state the synthesis method on their gemological reports, a quick analysis or a simple screening machine might give unclear results and not be sufficient to distinguish between mixed-growth diamonds and those grown using a single process.

Sean O'Neal and Guy Borenstein
Stuller Inc.
Lafayette, Louisiana

Diamond trader Ishaia Gol. It is always enlightening to encounter individuals who have left an indelible mark on the jewelry industry. Among these remarkable people is Ishaia Gol (figure 24), a multi-faceted diamond entrepreneur and owner of Ishaia Trading Corp. in New York.

In his early twenties, Gol arrived in New York in 1975 after five years of service in the Israeli army, including during the 1973 war. He had two goals: to attend New York University and start working with his older brother, David, who was in the gem and diamond business in Italy. David was the oldest of six brothers, and Gol was the youngest. To become a buyer in David's American office, Gol needed to become an expert in the trade, learn English, and earn a business degree as soon as possible.

Gol's merchant Jewish family originated in Afghanistan, where they bought furs and other goods in Russia and sold them locally. The family relocated to Israel shortly after it became a country in 1948. David began cutting diamonds in Israel, where this was a growing industry. But he became bored sitting at the cutting wheel for hours on end and started traveling to sell diamonds in 1956. He opened an office in Milan, and by 1960, he was buying sapphires, rubies, emeralds, and other colored stones from Mumbai. These were more profitable for him than diamonds, but they sold slowly. David then shifted his focus back to buying larger diamonds, frequently visiting New York to make purchases. With the opening of the New York office, David needed his brother to manage it.

At the start of his career, Gol's role was to purchase diamonds for distribution in Italy and throughout Europe. He balanced this responsibility with academic pursuits in New York, studying business at NYU and obtaining his Graduate Gemologist diploma in one of GIA's earliest New York classes. Throughout his studies, he took the F train daily from NYU to 47th Street, where he rapidly acquired the skills to saw, cut, and sort diamonds—all while learning English.

After obtaining his GG diploma, Gol would go to GIA's laboratory every morning to submit diamonds for grading and then ship them to his brother. GIA's "little office on 580 [Fifth Avenue]" was where he stood in line and chatted with other dealers. As demand grew, the laboratory expanded to two floors, with the second floor dedicated to diamonds under two carats and the tenth floor for larger stones. The lines on either floor were so long that submitting a diamond could take half a day. Dealers with diamonds in both size categories had to wait in two lines. Gol would arrive early and have his secretary hold his place

for hours. Some people even set up a business queueing for others. Gol recalled, "The corridors would be packed with hundreds. It was crazy!"

Gol quickly found himself immersed in New York's tight-knit gem community. Dealers and cutters would share coffee, jokes, and advice. As a newcomer, Gol sought their opinions on the stones he was considering. Once he established himself as a reputable gemologist, they soon asked for his advice. Gol's opinion was held in such high esteem that William Goldberg would consult him to resolve family disputes over stones. "We had an amazing friendship," Gol said of Goldberg. Lazar Wolf was another important influence: "He understood diamonds like no other person in the world," Gol noted.

As a dealer in New York in the late 1970s, Gol hired another gemologist. Since then, he has always had another staff gemologist, and as a team, they developed a formidable reputation. Dealers trusted Gol to check or even polish diamonds for them. One important assignment involved cleaning up the famous but badly bruised 41.37 ct Ashoka diamond. Gol also helped sell other important diamonds, including the 76.02 ct Archduke Joseph, with perfect D color and Internally Flawless clarity, which originated from the ancient Golconda mines of India. Gol's team attended major auctions, where they would study the offered diamonds for hours. Many of them did not carry a grading report. The team would buy some of these large diamonds, have them graded, and sell them for a good profit.

Gol's first recommendation for any aspiring gemologist who wants to work with big diamonds: "Dive headfirst into the world of auctions and gain confidence there. Don't be shy—attend them all, from quaint little affairs to bustling sales in Paris and beyond. Be willing to travel to the farthest corners of the globe to lay eyes on a single extraordinary stone." He also notes, "To truly understand a gemstone, it must be viewed under consistent conditions. Always carry the same portable light source, ensuring each diamond is seen in the same familiar glow. Examining all stones against a white, nonfluorescent plastic backdrop will help better compare their unique characteristics." Gol swears by his trusty tweezers, which he uses with 10× and 14× loupes, and a set of master stones he has used for color comparison for more than four decades.

Figure 24. Diamond entrepreneur Ishaia Gol, interviewed in June 2024. Photo by Pedro Padua.

Ishaia Gol's final piece of advice is to never stop learning. He urges aspiring gemologists to soak up as much education as possible: "Take every class you can get your hands on—it is the key to unlocking a successful career in this field."

This June 2024 interview with Ishaia Gol was captured on video as part of GIA's Oral History Project to be used by future historians. To see more, go to www.gia.edu/gems-gemology/summer-2025-gemnews-ishaia-gol.

Al Gilbertson
GIA, Carlsbad

TREATMENTS

Diffusion-induced blue spinel-like layer on natural sapphire. Recently, the GGTL laboratory in Geneva received three gems for identification weighing 1.43, 1.55, and 2.65 ct and exhibiting a blue coloration fairly typical of cobalt-bearing gems such as spinel (figure 25, left). Microscopic observation revealed the presence of inclusions, some

Figure 25. Left: Sapphires, weighing 1.43, 1.55, and 2.65 ct, diffused with cobalt and zinc, which formed a surface layer of blue spinel. Right: The 2.65 ct sample in immersion with brightfield illumination showing the typical spiderweb effect of diffused stones. Photos by Féodor Blumentritt.

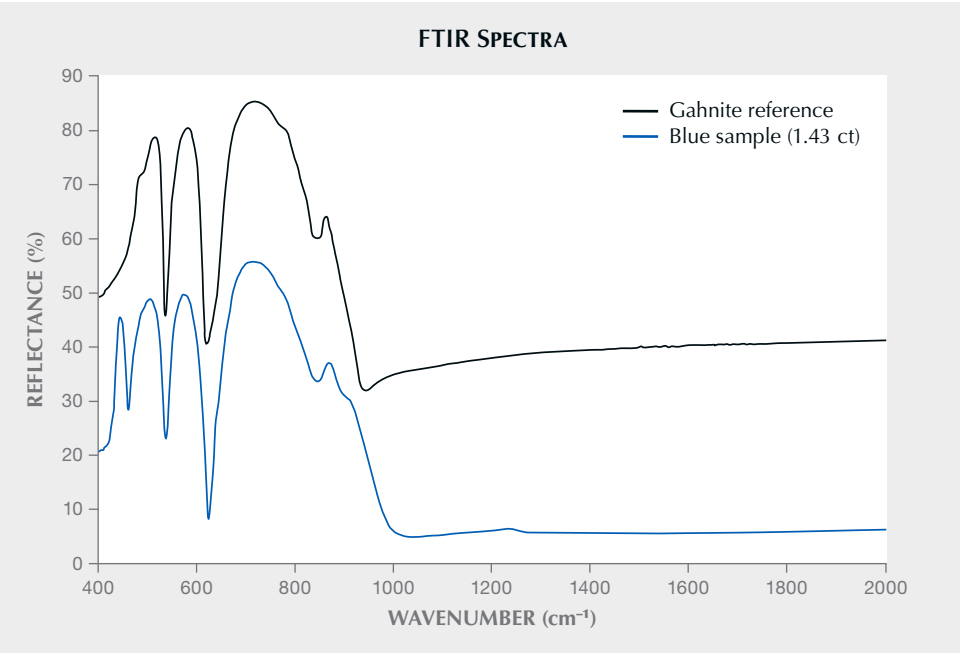

Figure 26. Infrared spectra in specular reflectance mode of a natural gahnite reference sample from Madagascar and the 1.43 ct blue sapphire sample. Spectra are offset vertically for clarity.

altered, such as rutile needles, mineral inclusions surrounded by discoidal fractures, and Rose channels. However, the surface condition and color zonation indicated the presence of diffusion. Some facets that were visibly unpolished following treatment displayed a granular appearance. In immersion fluid, it was observed that some of the edges and facets underwent repolishing, resulting in colorless surfaces (figure 25, right). On one of the stones, the color zonation was clearly visible on the surface of the facets and appeared as a cloudy pattern.

The identification of these stones by means of specular reflectance infrared spectroscopy demonstrated a clear correlation with gahnite ($ZnAl_2O_4$; figure 26). However, analysis of the stones' luminescence under long-wave

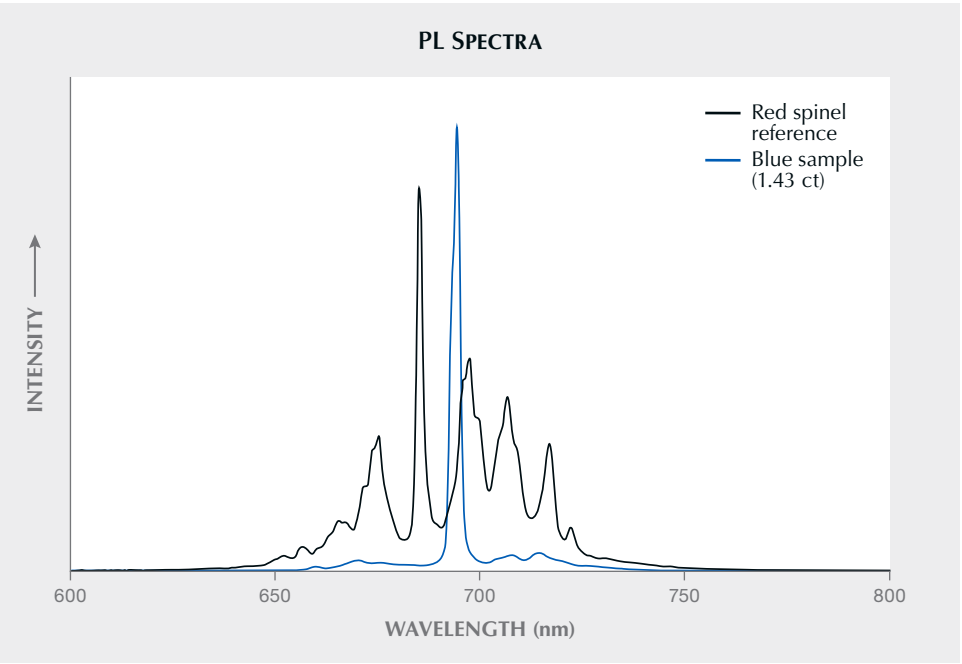

Figure 27. Typical luminescence spectrum of a red spinel reference sample compared with the luminescence spectrum of the 1.43 ct blue sapphire sample that matched the usual luminescence of Cr^{3+} in corundum. Note that the resolution of the spectrometer was not high enough to distinguish the two R1 and R2 transitions at about 694 nm.

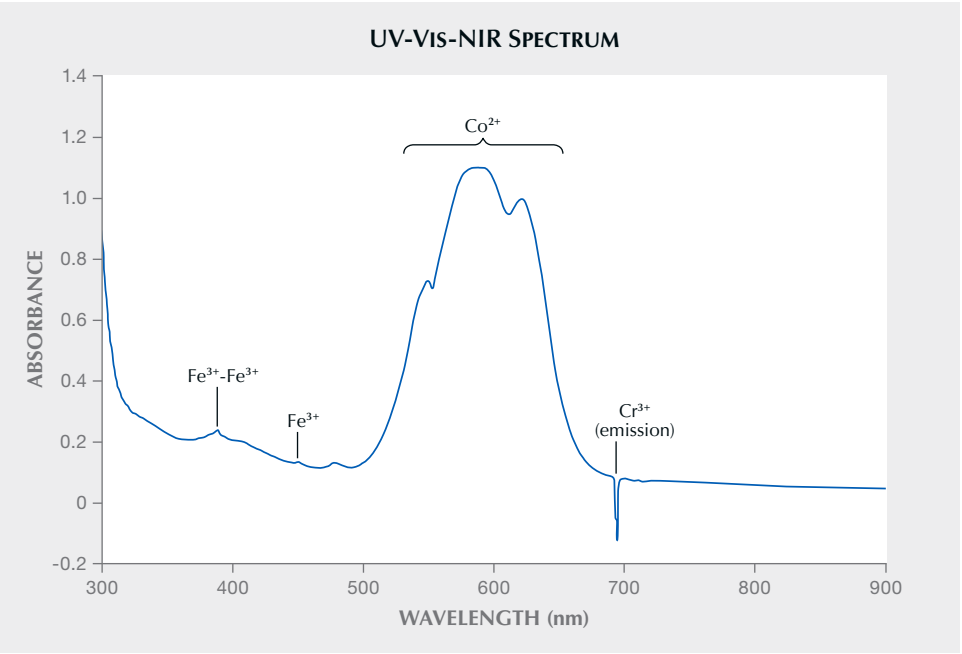

Figure 28. Absorption spectrum of the 1.43 ct sample showing characteristic features of Co^{2+} usually measured in spinel, superimposed to usual iron absorption features of sapphire.

ultraviolet (365 nm) light revealed a Cr^{3+} luminescence spectrum, characteristic of an octahedral environment in corundum (T. Kushida and Y. Tanaka, "Direct optical excitation into excited states of Cr^{3+} pairs in ruby," *Solid State Communications*, Vol. 11, No. 10, 1972, pp. 1341–1344), rather than in spinel structure (figure 27; see e.g., I. Malíčková et al., "Optical and luminescence spectroscopy of varicolored gem spinel from Mogok, Myanmar and Lục Yên, Vietnam," *Minerals*, Vol. 11, No. 2, 2021, article no. 169). This luminescence was homogeneous across the stones, and it was confirmed that it did not emanate solely from the surface by illuminating the colorless zonation of the stones. The results of an energy-dispersive X-ray fluorescence semi-quantitative chemical analysis provided evidence to support the inconsistency between the infrared spectrum and luminescence, with a majority proportion of aluminum (~89.9 wt.% of Al_2O_3) and, to a lesser extent, zinc (~6.5 wt.% of ZnO). The proportions of the two elements do not correspond to a spinel structural formula. Instead, they were consistent with the hypothesis of the coexistence of spinel and corundum structures.

Moreover, the detection of large quantities of cobalt (~3.4 wt.% of Co_3O_4) was consistent with the ultraviolet/visible/near-infrared (UV-Vis-NIR) absorption spectrum, supporting cobalt as the main cause of color (figure 28; D.K. Sardar et al., "Spectroscopic properties of Co^{2+} in related spinels," *Journal of Applied Physics*, Vol. 91, No. 8, 2002, pp. 4846–4852). A previous publication already documented "cobalt-diffused sapphires" (R.E. Kane et al., "The identification of blue diffusion-treated sapphires," Summer 1990 *G&G*, pp. 115–133), but the presence of Co^{2+} in a corundum structure remained unclear despite a parallel made with the color of cobalt-blue synthetic spinel. One later article (Summer 2002 Gem Trade Lab Notes, p. 167) discussed a possible interaction of cobalt with the corundum surface without being more specific.

The aforementioned analyses led to the identification of these stones as natural sapphire partly owing to the typical Cr^{3+} luminescence. These sapphires likely underwent an attempt at diffusion of zinc and cobalt, resulting in the crystallization of a layer of blue spinel structure (gahnite) on the surface, which was identified by reflectance infrared spectroscopy. This treatment serves to demonstrate the considerable inventiveness required to induce a cobalt-bearing spinel color in corundum.

Féodor Blumentritt, Guillaume Zuber, Candice Caplan, and Franck Notari
GGTL Laboratories, Switzerland